Mathematical modeling and thermal performance analysis of shallow experimental cooling ponds

Sami Al-Sanea[a], Jamel Orfi[b],*

[a]*Department of Mechanical Engineering, College of Engineering, King Saud University, P.O. Box: 800, Riyadh 11421, Saudi Arabia, Tel. +966-11-467-6682; Fax: +966-11-467-6652; email: sanea@ksu.edu.sa*
[b]*Department of Mechanical Engineering, College of Engineering, King Saud University, P.O. Box: 800, Riyadh 11421, Saudi Arabia, Tel. +966-11-467-9798; Fax: +966-11-467-6652; email: orfij@ksu.edu.sa*

a b s t r a c t

A numerical study is conducted to simulate flow and heat transfer in shallow cooling ponds. A depth-integrated CFD model, based on the finite-volume method, is developed and applied to calculate detailed velocity and temperature distributions inside the pond. The numerical model is validated by comparing results with temperature measurements available for an experimental cooling pond. The model is used to investigate effect of mass flow rate ($\dot{m}$) on pond hydrodynamics and thermal characteristics for cases of without and with internal baffles. The results show that the pressure loss coefficient remains constant, while the pressure drop between pond inlet and outlet increases with increasing $\dot{m}$. The heat dissipated from the pond at the air–water interface increases with $\dot{m}$ despite the decrease in difference between water inlet and outlet temperatures. The pond effective heat-transfer coefficient, pond mean temperature, and water loss by evaporation are determined as a function of $\dot{m}$ and relative humidity. The outlet temperature from the pond is determined as a function of pond cooling capacity. Streamline plots show that the flow pattern is independent of $\dot{m}$ but is strongly dependent on geometric configuration. A single contour map of normalized speed is, therefore, sufficient to describe all speeds inside the pond for different $\dot{m}$. It is recommended that $\dot{m}$ should be as high as possible in order to enhance heat transfer from the pond but this would increase pumping power of cooling water through condenser tubes in which a compromise must be sought.

Keywords: Shallow cooling ponds; Heat transfer characteristics; Water evaporation; Depth-integrated model; CFD simulation

1. Introduction

The efficiency of industrial plants such as chillers, steam power and desalination plants depends strongly on the effectiveness of their heat and/or mass rejection systems. Reducing the condensing temperature of steam power plants and chillers increases turbine work obtained in the former, and reduces compressor work and increases refrigeration effect in the latter. For desalination plants, effective brine discharge reduces adverse impacts on marine environment and increases the performance of the plants. Usually for power plants and chillers heat is rejected to either water or ambient air. Water-cooled condensers are generally preferred to air-cooled condensers since they can remove much more heat, produce lower condensing temperatures and therefore provide higher energy efficiency. Besides, concentrated brine exiting from desalination plants is usually diluted with natural seawater, power plant cooling waters or municipal wastewaters [1] in order to reduce its salt content and temperature prior to discharge.

There are several methods of heated water and brine disposal from power and desalination plants [1–4]. However, the natural and easy way is "the once through method" for

* Corresponding author.

which the exited water from the plants is discharged directly to the receiving water body.

For seawater desalination plants located in general near the coast, the widely used method is to discharge the brine back to the sea through pipes or submarine emissaries [5]. This once through method is known to be in general effective but it can generate several additional problems such as possible recirculation of the heated and more concentrated brine effluents, adverse ecological effects on marine environment and non-conformity with the existing environmental regulations. In fact, environmental rules and regulations are becoming stricter and demanding. González et al. [6] reported that recent European environmental legislations oblige plant operators to assume costs associated with potential damage of the used disposal methods. On the other hand, when the once through method is not used such as when a natural water body is not available, operations with closed cycle modes are the alternatives. These are either cooling towers, cooling ponds, or combination of both [7,8].

Cooling ponds, which are large man-made bodies of water open to ambient air, do not need any maintenance and can provide recreational, aesthetic, and ecological values to the community. Watanabe and Connor [9] reported that cooling ponds offer several advantages over cooling towers including low maintenance, low power requirements, esthetic, and less environmental effects. Operations with closed cycle modes present several advantages. For instance, power and thermal desalination plants use cooling ponds to decrease the temperature of the cooling water or the brine leaving the plants before discharging it back into the sea. Solar evaporation is commonly used for brine disposal especially for inland reverse osmosis desalination plants in arid and semi-arid regions [10].

The performance of cooling ponds depends on a number of parameters such as the surface area, ambient air temperature and humidity, wind speed and direction, solar heat gain, water flow rate, and temperature. The pond geometrical configuration and depth are also important. Many cooling ponds are shallow thereby allowing good vertical mixing. Ahmed et al. [10] reported depths ranging from 25 to 45 cm as optimal for maximizing the evaporation rates. The use of baffles in such ponds to increase the actual hydraulic retention time and enhance cooling mechanisms has been suggested and considered in several applications and studies [1,11]. Lowe [1] noticed that previous studies on internal baffles focused on the horizontal positioning of the baffles. The author conducted an experimental investigation using vertical and underflow baffle arrangements. The results showed an improvement in cooling of over 30%.

Baffles have also been used in water treatment technologies [12–14]. Using CFD model, Wei et al. [12] investigated the effect of guiding baffles downstream from surface aerators on the flow field in an oxidation ditch. The results showed that the installation of the guiding baffles increased the efficiency of oxygen transfer. Furthermore, it is well understood that baffles have beneficial impacts on the design and construction of sedimentation tanks specifically on the hydraulic characteristics and the solid removal rates. However, several other questions such as the appropriate horizontal position and submerged depth of the baffles require closer and deeper analysis. Liu et al. [13] focused on

effects of geometrical characteristics of baffles using a solid–liquid two-phase equations and *k*-epsilon turbulence model. Hussein et al. [14] conducted a numerical study to evaluate the impact of geometrical characteristics of a baffle on the performance of an oil and water gravity separator tank. The results showed that the flow field patterns, expressed in streamlines and velocity profiles, were function of baffle location and structure.

On the other hand, hydraulic ponds are found in several other applications such as in the chemical biological treatment of contaminated water and solar energy storage. Ogarekpe and Agunwamba [15] studied the effect of surface area on performance of integrated solar and hydraulic jump enhanced waste stabilization pond. Besides, studies of increasing number are being conducted on the thermal performance of solar ponds, their design characteristics, stability, and limitations [16–18]. Suarez et al. [19] analyzed numerically the 2-D coupled transient double diffusion convection for salt gradient solar ponds. They incorporated evaporation and sensible heat losses, and solar and longwave radiation fluxes at water–air interface. The accurate evaluation of evaporation rate is essential in modeling evaporation from solar ponds. Sartori [20] reviewed several empirical correlations used for calculation of evaporation rate from large free water surfaces and noticed a large scattering between published studies. The author addressed attention to the pan evaporation and concluded that it might generate considerable differences in relation to a large water surface evaporation, depending on surface length and rate of mass transfer.

The present paper investigates the effect of mass flow rate and humidity of ambient air on the performance of a small-size, shallow experimental cooling pond by using a 2-D numerical model. The numerical model solves the depth-integrated momentum and energy equations employing the finite volume procedure. The effect of using baffles is also investigated. The decision to use such a small pond was instigated by the availability of a good set of experimental data, which facilitates the validation of the model and assessing its accuracy. The trends obtained for that pond should hold true to real life size ponds.

2. Mathematical formulation

2.1. Flow situation

The experimental cooling pond considered in this study is shown schematically in Fig. 1. Heated water enters the pond and gets cooled by heat rejection at the air–water interface. The pond is of a rectangular shape 10.9 m × 5.4 m. The inlet is 0.275 m and the outlet is 0.45 m wide. The depth of flow is uniform at 0.0762 m. This corresponds to an experimental cooling pond setup of Cerco [21] in which temperature measurements were reported for two mass flow rates for cases without and with baffles. Measurements in the study by Cerco [21] were reported in the imperial system of units and, hence, converted in the present study to the metric system.

It is noted that temperature measurements conducted by Cerco [21] are relevant to shallow water equations where vertical variations of temperature are very small. Under these
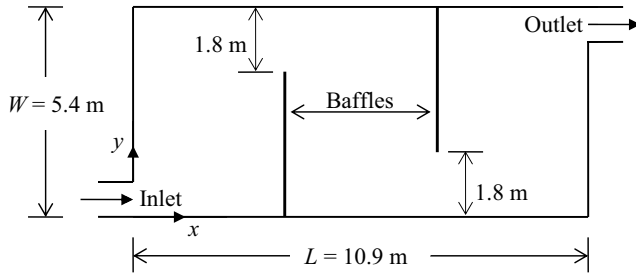
Fig. 1. Geometrical configuration of the cooling pond, plan view.

conditions, the use of a depth integrated numerical model is justified. The temperatures used in the present study are under steady state and measured at the surface.

2.2. Governing equations

Under steady-state conditions, hydrostatic pressure distribution, and applying the "rigid-lid" approximation, the following depth-integrated equations are used as applicable to shallow-water flows. Depth-averaged values are, hence, assumed for all dependent variables.

2.2.1. Conservation of mass

$$\frac{\partial}{\partial x}\left(z\overline{u}\right) + \frac{\partial}{\partial y}\left(z\overline{v}\right) = 0 \tag{1}$$

where $\overline{u}$ and $\overline{v}$ are the depth-averaged velocity components in the x- and y-directions, respectively, and z is the local depth of flow.

2.2.2. Conservation of u-momentum

$$\frac{\partial}{\partial x}\left(z\overline{u}^2\right) + \frac{\partial}{\partial y}\left(z\overline{u}\,\overline{v}\right) - \frac{1}{\rho}\frac{\partial}{\partial x}\left(z\overline{\mu}_{eff}\frac{\partial \overline{u}}{\partial x}\right) - \frac{1}{\rho}\frac{\partial}{\partial y}\left(z\overline{\mu}_{eff}\frac{\partial \overline{u}}{\partial y}\right) = S_u \tag{2}$$

where ρ is water density, $\overline{\mu}_{eff}$ is effective viscosity and S_u is source term given by:

$$S_u = -\frac{z}{\rho}\frac{\partial p}{\partial x} + zf\overline{v} - C_f\overline{u}\left(\overline{u}^2 + \overline{v}^2\right)^{1/2} + C_s\frac{\rho_{air}}{\rho}U_o\left(U_o^2 + V_o^2\right)^{1/2} \tag{3}$$

where p is static pressure, f is Coriolis parameter, C_f is bed friction factor, C_s is wind force friction factor, ρ_{air} is air density, U_o and V_o are wind relative velocities with respect to water velocity in the x- and y-directions, respectively.

2.2.3. Conservation of v-momentum

$$\frac{\partial}{\partial x}\left(z\overline{u}\,\overline{v}\right) + \frac{\partial}{\partial y}\left(z\overline{v}^2\right) - \frac{1}{\rho}\frac{\partial}{\partial x}\left(z\overline{\mu}_{eff}\frac{\partial \overline{v}}{\partial x}\right) - \frac{1}{\rho}\frac{\partial}{\partial y}\left(z\overline{\mu}_{eff}\frac{\partial \overline{v}}{\partial y}\right) = S_v \tag{4}$$

where S_v is source term and is given by:

$$S_v = -\frac{z}{\rho}\frac{\partial p}{\partial y} - zf\overline{u} - C_f\overline{v}\left(\overline{u}^2 + \overline{v}^2\right)^{1/2} + C_s\frac{\rho_{air}}{\rho}V_o\left(U_o^2 + V_o^2\right)^{1/2} \tag{5}$$

2.2.4. Conservation of energy

$$\frac{\partial}{\partial x}\left(z\overline{u}\,\overline{T}\right) + \frac{\partial}{\partial y}\left(z\overline{v}\,\overline{T}\right) - \frac{1}{\rho}\frac{\partial}{\partial x}\left(z\frac{\overline{\mu}_{eff}}{\sigma_T}\frac{\partial \overline{T}}{\partial x}\right) - \frac{1}{\rho}\frac{\partial}{\partial y}\left(z\frac{\overline{\mu}_{eff}}{\sigma_T}\frac{\partial \overline{T}}{\partial y}\right) = \frac{S_T}{c_p} \tag{6}$$

where $\overline{T}$ is depth-averaged temperature, σ_T is turbulent Prandtl number ($= c_p\mu_{eff}/k_{eff}$), c_p is specific heat, k_{eff} is the effective thermal conductivity, and S_T is source (or sink) term and represents energy interaction at the air–water interface. Convection, radiation, and evaporation effects are accounted for through this S_T term. Details of heat flux components at air–water interface are given in Section 2.6.

2.2.5. Common form of transport equation

All the above governing equations can be recast in a common form of a single general transport equation given below, enabling one solution procedure for all equations.

$$\frac{\partial}{\partial x}\left(z\overline{u}\,\overline{\phi}\right) + \frac{\partial}{\partial y}\left(z\overline{v}\,\overline{\phi}\right) - \frac{1}{\rho}\frac{\partial}{\partial x}\left(z\overline{\Gamma}_{eff,\phi}\frac{\partial \overline{\phi}}{\partial x}\right) - \frac{1}{\rho}\frac{\partial}{\partial y}\left(z\overline{\Gamma}_{eff,\phi}\frac{\partial \overline{\phi}}{\partial y}\right) = S_\phi \tag{7}$$

where $\overline{\phi}$ is general depth-averaged variable and stands for 1, $\overline{u}$, $\overline{v}$, and $\overline{T}$ in governing equations, respectively; $\overline{\Gamma}_{eff,\varnothing}$ is effective exchange (diffusion) coefficient and stands for 0, $\overline{\mu}_{eff}$, $\overline{\mu}_{eff}$, and $\overline{\mu}_{eff}/\sigma_T$ in governing equations, respectively; and S_ϕ is source/sink of $\overline{\phi}$.

2.3. Boundary conditions

All dependent variables $\overline{u}$, $\overline{v}$, and $\overline{T}$ or their derivatives must be prescribed on all boundaries. In mathematical form, these boundary conditions are specified as follows:

2.3.1. Solid boundaries and internal baffles

Velocity components and normal temperature gradient are set to zero.

2.3.2. Inlet port

Velocity is fixed according to inlet port area and total mass flow rate. Temperature equals that of the heated water coming out of condenser.

2.3.3. Outlet port

Velocity is fixed according to outlet port area and total mass flow rate. However, temperature at outlet port is unknown and is calculated by the iterative solution procedure.

It is noted that in the current 2D depth-integrated model, the interaction at the air–water interface is accounted for by source/sink terms present in the governing equations. Details of convection, radiation, and evaporation heat-flux components at the air–water interface are given in Section 2.6.

2.4. Turbulence modeling

The effective-viscosity coefficient appearing in Eqs. (2)–(7) is calculated from a mixing-length turbulence model in which the turbulent viscosity is related to a mixing length and a mean velocity gradient across pond width. This very

simple model is used since in shallow water flows the bottom friction and wind stress dominate over the diffusion process. Accordingly, the diffusion contribution in shallow water equations is relatively weak and, hence, the diffusion terms may be disregarded, see for example Vreugdenhil [22]. However, these terms are retained in the present study and are modeled by a constant eddy viscosity (μ_t) calculated from the following mixing length formula:

$$\mu_t = \rho \, l^2 \left| \frac{\partial U}{\partial y} \right| \tag{8}$$

where l is the mixing length taken equal to 5% the pond length (L), and $\frac{\partial U}{\partial y}$ is the mean velocity gradient across the pond width.

2.5. Numerical algorithm

The CFD technique hinges on representing the differential equations in numerical form. The finite volume approach is used in the present study Patankar [23]. The pressure field and velocities are determined by the well-known SIMPLE algorithm of Patankar and Spalding [24].

2.5.1. Major solution steps

Numerical procedures based on the finite-volume method share the same general features but differ in specific details regarding the discretization process and the solution algorithm. The major solution steps are described as follows:

- Flow domain is divided into discrete regions by constructing a finite-volume grid.
- Governing differential equations are transformed into finite-volume equations by integration over control volumes [23].
- Finite-volume equations are solved by Tri-Diagonal Matrix Algorithm (TDMA).
- Pressure field is determined by the SIMPLE algorithm [24] in which corrections based on mass continuity requirements are made to velocities obtained from solution of momentum equations. By successive solution of momentum and pressure correction equations, velocity, and pressure fields are determined.

2.5.2. Finite-volume equations

In a staggered grid-system arrangement, compass notations N, S, E, and W are used to identify neighboring nodes that surround a typical finite-volume central node P. Values of pressure and scalar variables (e.g., temperature) are stored at these nodal points. The velocities are located halfway between these nodes, that is, at cell faces identified by n, s, e, and w.

2.5.2.1. General form

All finite-volume equations can be cast in terms of a general variable ϕ, where ϕ stands for velocity components u and v, temperature T, and pressure correction. Differences in contents of each equation are contained in source terms.

General form of the finite-volume equation linking value of ϕ at P to those at N, S, E, and W is obtained as [23]:

$$\phi_P = \frac{A_N^\phi \phi_N + A_S^\phi \phi_S + A_E^\phi \phi_E + A_W^\phi \phi_W + S_P^\phi}{A_N^\phi + A_S^\phi + A_E^\phi + A_W^\phi - S_P^{\phi/}} \tag{9}$$

or, in a more compact form as:

$$\phi_P = \frac{\sum_i^{N,S,E,W} \left(A_i^\phi \phi_i \right) + S_P^\phi}{\sum_i^{N,S,E,W} A_i^\phi - S_P^{\phi/}} \tag{10}$$

where $\sum_i^{N,S,E,W}$ is summation over neighboring nodes, N, S, E, and W; A_i^ϕ are finite-volume coefficients (A_N^ϕ, A_S^ϕ, A_E^ϕ, and A_W^ϕ) of variable ϕ and express effects of diffusion and convection.

Eqs. (9) or (10) are written for each variable at every grid point and, hence, algebraic equations are obtained for all variables at all grid points which can be solved by any standard solution algorithm.

2.5.2.2. Source term

In Eqs. (9) and (10), source term S_ϕ is linearized and expressed as follows:

$$S_\phi V_P = S_P^\phi V_P + S_P^{\phi/} \phi_P V_P \tag{11}$$

where V_p is volume of finite-volume cell, S_P^ϕ and $S_P^{\phi/}$ are "linearized source" coefficients. It is noted that all physical effects present in the governing equations, apart from the convection and diffusion terms, are introduced through the source term. Besides, speed of convergence and stability of numerical solution depend strongly on how the source term is formulated. For suitable forms of introducing different physical effects into source/sink terms, the reader may refer to Patankar [23].

Source terms are also utilized to introduce effects of internal obstacles on flow and temperature fields by appropriate modifications made to the S_P^ϕ and $S_P^{\phi/}$ coefficients in Eq. (11). In the present study, the presence of baffles in the cooling pond is handled through these coefficients to ensure that normal velocity components at these obstructions are equal to zero, while those components adjacent and parallel to the obstructions undergo shear stress effects.

2.5.3. Solution of finite-volume equations

The finite-volume equations are linearized and solved by an iterative process. Thus, the final solution is obtained after a number of iterations and by re-evaluating values of finite-volume coefficients at every iteration. In the present computer program which is written in FORTRAN, the equations are solved simultaneously on a line-by-line basis by the Tri-Diagonal Matrix Algorithm (TDMA). The main solution steps are summarized as follows:

(i) Guess values of variables in the field.
(ii) Compute values of u on a line by solving the finite volume form of the u-momentum equation.

(iii)   Compute values of v as in (ii) above.
(iv)   Compute values of T on the line.
(v)   Compute values of pressure correction by employing mass continuity errors produced by u's and v's obtained from steps (ii) and (iii).
(vi)   Correct pressures and velocities on the line.
(vii) Move to next line and repeat steps (ii) to (vi) for the whole field.
(viii) Repeat iteration of whole field until convergence is reached.

2.5.4. Convergence and stability of procedure

Convergence is monitored through use of residuals. A residual of a variable ϕ at a node P, denoted by R_P, is defined, with reference to Eq. (10) by:

$$R_P = \phi_P A_P^\phi - \sum_i \left(A_i^\phi \phi_i \right) - S_P^\phi \tag{12}$$

where ϕ_P is the value at the previous iteration, and the summation is over the four node faces.

All residuals are suitably normalized and a solution that produces sufficiently small field residuals (less than 10^{-4}), for all variables, is regarded as a converged one. This is provided that the field values of variables solved do not change by more than about 0.01% during successive iterations.

As to the stability of the procedure, it is found that the use of under-relaxation factors (β, where $\beta < 1$) is necessary. This is done as follows:

$$\phi_{\text{new}} = \beta \phi^* + \left(1 - \beta \right) \phi_{\text{old}} \tag{13}$$

where ϕ^* is the value of ϕ that is just being solved. The value of β is 0.5 for all variables.

2.6. Heat flux components at air–water interface

The ultimate heat rejection from the pond takes place from the pond surface to the ambient air and surroundings. The net interchange is made up of the following components: (i) evaporation heat loss q_e, (ii) emitted longwave back radiation q_{br}, (iii) incident surroundings radiation q_{sur}, (iv) reflected surroundings radiation $q_{sur,r}$, and (v) sensible heat loss to atmosphere q_c. The latter consists of both forced ($q_{c,f}$) and natural convection heat transfer ($q_{c,n}$). Thus, the net heat transfer from the pond (q) is given by:

$$q = q_e + q_{br} - q_{sur} + q_{sur,r} + q_c \tag{14}$$

It is noted that ($q_{br} - q_{sur} + q_{sur,r}$) represents net loss by longwave radiation and that q must balance the thermal loading on the pond.

The above components are usually expressed by empirical correlations (as presented next) and are function of ambient air temperature and relative humidity, wind speed, and water surface reflectivity and emissivity. The sum of these components may be written as:

$$q = h_m A_s \Delta T_m \tag{15}$$

where h_m is the pond mean effective heat-transfer coefficient, A_s is the pond surface area, and $\Delta T_m = T_m - T_{eq}$ is the temperature difference between pond mean water temperature and the equilibrium water temperature (T_{eq}). T_{eq} results from natural environmental conditioning when there is no plant-imposed loading, more details are given later.

2.6.1. Evaporation heat loss (q_e)

A general correlation relating the mass flux at air–water interface (M in kg/m² s) to water vapor mass fraction (m) is [25]:

$$M = \text{St } \rho_{\text{air}} V_{\text{rel}} \left(m_{\text{surf}} - m_{\text{atm}} \right) \tag{16}$$

where St is Stanton number (= $h / \rho_{\text{air}} \times V_{\text{rel}} \times c_p$), V_{rel} is relative velocity of wind and water, m_{surf} and m_{atm} are mass fraction of water vapor in air at surface and in atmosphere. The mass fraction m_{surf} is a function of water temperature (T) and total pressure (p_{tot}).

A specific correlation used in the present study is [26,27] as follows:

$$M = \rho_{\text{air}} \left(a + b V_{\text{rel}}^c \right) \left(m_{\text{surf}} - m_{\text{atm}} \right) \tag{17}$$

where $a = 0.0042$, $b = 0.0057$, and $c = 0.82$.

The evaporation heat loss is then:

$$q_e = M L \tag{18}$$

where L is the latent heat of vaporization (J/kg).

The amount of water evaporated in terms of height of water in mm/d is as follows:

$$z_e = 8.64 \times 10^7 M / \rho \tag{19}$$

2.6.1.1. Mass fraction of water vapor m vs. saturation temperature T

In a mixture of steam and air, the total pressure (p_{tot}) is given by:

$$p_{\text{tot}} = p_{\text{air}} + p_{\text{vap}} \tag{20}$$

where p_{air} is air partial pressure and p_{vap} is vapor partial pressure; p_{tot}, p_{vap}, and m are related thermodynamically by:

$$p_{\text{vap}} = \frac{p_{\text{tot}}}{0.378 + \dfrac{0.622}{m}} \tag{21}$$

Taking p_{tot} at 1 atm (= 1,013.25 m bar), then:

$$m = \frac{0.622}{\dfrac{1013.25}{p_{\text{vap}}} - 0.378} \tag{22}$$

where p_{vap} is water vapor pressure (in mbar) and is equal to ϕp_{sat} at same temperature.

Considering a temperature range between 10°C and 54°C, p_{vap} is fitted to the temperature (T) by a logarithmic relation as follows:

$$\log_{10}\left(p_{\text{vap}}\right) = \frac{a_1 + a_2 T}{1 + a_3 T} \qquad (23)$$

where T is the saturation temperature in °C. Using the steam table, the following values of coefficients are determined: $a_1 = 0.78588$, $a_2 = 0.03491$, and $a_3 = 0.00421$. Therefore, by substituting values of T, p_{vap} are calculated, which in turn determine values of m. The latter values are then used to determine M and q_e.

2.6.2. Incident surroundings radiation (q_{sur})

The longwave radiation from the surrounding is assumed to obey the Stefan–Boltzmann law with the emissivity of the laboratory equals to 0.97. Thus:

$$q_{\text{sur}} = \varepsilon \, \sigma T_{\text{sur}}^4 \qquad (24)$$

where $\sigma = 5.67 \times 10^{-8}$ W/m² K⁴ and T_{sur} is the surroundings temperature (K).

2.6.3. Reflected surroundings radiation ($q_{sur,r}$)

This is the amount of the incoming surroundings radiation that is being reflected by the water surface. It is equal to $(R \cdot q_{\text{sur}})$, where $R = 0.03$ is the reflectivity of the water surface.

2.6.4. Emitted longwave back radiation (q_{br})

The outgoing radiation flux from water surface is given by the Stefan–Boltzmann law with emissivity of water surface equals to 0.97. Thus:

$$q_{\text{br}} = 0.97 \sigma T^4 \qquad (25)$$

where T is local water temperature in Kelvin.

2.6.5. Sensible heat loss to atmosphere (q_c)

The convection heat transfer out of the surface is the sum of the wind driven forced convection ($q_{c,f}$) and the buoyant natural convection ($q_{c,n}$).

2.6.5.1. Forced convection

A general correlation relating $q_{c,f}$ to temperature difference is [25] as follows:

$$q_{c,f} = \text{St} \, \rho_{\text{air}} V_{\text{rel}} c_{p,\text{air}} \left(T - T_{\text{air}}\right) \qquad (26)$$

where St is Stanton number, $c_{p,\text{air}}$ is specific heat of air, and T_{air} is air temperature. A more specific correlation used in the present study is [26,27] as follows:

$$q_{c,f} = 6.88 V_{\text{rel}}^{0.82} \left(T - T_{\text{air}}\right) \qquad (27)$$

2.6.5.2. Natural convection

Generally, $q_{c,n}$ is correlated to temperature difference by [25]:

$$q_{c,n} \approx 1.6 \left(T - T_{\text{air}}\right) \left(\left|T - T_{\text{air}}\right|\right)^{1/3} \qquad (28)$$

A more specific correlation is used in the present study as given by [26,27] as follows:

$$q_{c,n} = 5.06 \left(T - T_{\text{air}}\right) \qquad (29)$$

3. Simplified 1-D closed form analytical solutions

Closed-form analytical solutions can be affected for simplified 1-D pond models. These solutions are useful for design approximations or preliminary estimates [28]. In the present study, these analytical solutions are also used for comparisons with corresponding numerical results for the purpose of validating the numerical model under simplified situations.

3.1. Physical situation and basic assumptions

A simple 1-D pond with constant water depth is considered. Exact analytical solutions for the temperature distribution and cooling capacity of the pond are limited to situations where steady-state, uniform velocity, constant properties, and constant surface heat-transfer coefficient assumptions are made.

3.2. Governing equations

Based on the above simplifying assumptions, Eqs. (1)–(6) are reduced to:

3.2.1. Mass continuity

$$\frac{du}{dx} = 0 \qquad (30)$$

3.2.2. u-momentum

$$\frac{dp}{dx} = 0 \qquad (31)$$

3.2.3. Energy conservation

$$u\frac{dT}{dx} - \alpha\frac{d^2 T}{dx^2} = -\frac{q_s^{//}}{\rho c_p z} \qquad (32)$$

where α is thermal diffusivity (dispersion coefficient), m²/s, $= \dfrac{k}{\rho c_p} = \dfrac{\mu}{\rho \sigma_T}$, and $q_s^{//}$ is heat flux from water body (W/m²) given by:

$$q_s^{//} = h\left(T - T_{\text{eq}}\right) \qquad (33)$$

where h is the heat-transfer coefficient (W/m² K).

Eq. (32) is a second-order ordinary differential equation for which analytical solutions can be derived for different degrees of mixing as follows.

3.2.3.1. Finite mixing

The solution for the dimensionless outlet temperature from the pond θ_o is given by:

$$\theta_o = \frac{T_o - T_{eq}}{T_i - T_{eq}} = \frac{4a \exp\left(\dfrac{1}{2\alpha^*}\right)}{\left(1+a\right)^2 \exp\left(\dfrac{a}{2\alpha^*}\right) - \left(1-a\right)^2 \exp\left(\dfrac{-a}{2\alpha^*}\right)} \tag{34}$$

where

$$a = \left(1 + 4r\,\alpha^*\right)^{1/2} \quad \text{is a dimensionless parameter,} \tag{35}$$

$$\alpha^* = \frac{\alpha}{u\,L} \quad \text{is a dimensionless dispersion coefficient,} \tag{36}$$

$$r = \frac{hA_s}{\dot{m}c_p} \quad \text{is a dimensionless cooling capacity parameter,} \tag{37}$$

u is pond cross-sectional mean velocity (m/s), L is pond length (m), A_s is pond surface area (m²), and $\dot{m}$ is the mass flow rate through pond (kg/s).

3.2.3.2. No mixing (plug flow)

In a "plug flow" pond, there is no mixing between the heated discharge and the receiving water body and there is no dispersion along the flow path. The dispersion coefficient α and hence α^*, given by Eq. (36), are both zero. Accordingly, the energy equation is reduced to:

$$u\frac{dT}{dx} = -\frac{q_s^{//}}{\rho c_p z} \tag{38}$$

in which its analytical solution is the classic exponential decay equation given by:

$$\theta_o = \exp\left(-r\right) \tag{39}$$

where r is given by Eq. (37). In the numerical model, a no-mixing condition is achieved by setting the viscosity $\mu = 0$.

3.2.3.3. Complete mixing (fully mixed)

In a "fully mixed" pond, the inflow is immediately mixed and dispersed throughout the pond. This situation corresponds to infinite entrance mixing and dispersion in which α^* and $\mu \to \infty$. The analytical solution is given by:

$$\theta_o = \frac{1}{1+r} \tag{40}$$

In the numerical model, complete mixing is achieved by setting $\mu = a$ large value.

4. Results and discussion

All results produced by the iterative procedure were checked and considered to be fully converged when normalized field residuals fall below 10^{-4} and values of all variables cease to change with further iterations. A grid-independence check is demonstrated in Section 4.3, followed by numerical model validation. However, the specific cases investigated and the concept of the equilibrium temperature is described first.

4.1. Pond geometric configuration and cases studied

The flow situation was briefly described in Section 2.1 and schematically presented in Fig. 1. In the present study, two geometric configurations are considered namely, without and with internal baffles. For each configuration, two flow rates are used which correspond to the experimental values of 0.284 and 0.568 kg/s, Cerco [21]. Thus, numerical model predictions and measured results are presented and compared for four cases designated, in the present study, as Cases 1 through 4. These are: Case 1 for the lower flow rate without baffles, Case 2 for the lower flow rate with baffles, Case 3 for the higher flow rate without baffles, and Case 4 for the higher flow rate with baffles. It is to be noted that other geometric configurations had been investigated experimentally by Cerco [21] and that the author reported the bulk of temperature measurements by way of contours. Of particular interest is the value of the outlet temperature from the pond.

In the present study, further results are obtained by varying the mass flow rate ($\dot{m}$) over a wider range than that used in the experiments. Thus, by conducting a parametric study, the pond cooling capacity is correlated with the pond outlet temperature through changing $\dot{m}$ for the two cases of without and with baffles. Numerical model predictions are also carried out in order to investigate effects of varying the relative humidity (ϕ) since the evaporation rate, a major component of cooling at the air–water interface, is so much dependent on ϕ.

4.2. Equilibrium temperature and pond effective heat-transfer coefficient

The equilibrium temperature (T_{eq}) is a theoretical temperature used as a reference in the definition of the dimensionless temperature (θ) and in calculating the pond mean effective heat-transfer coefficient (h_m) and the pond cooling capacity (r). T_{eq} is determined from an energy balance applied at the air–water interface in the absence of an external load on the pond, in which case heat lost by evaporation is balanced by heat gained by convection (both forced and natural) and net radiation exchange. Values of T_{eq} are calculated iteratively and are displayed in Fig. 2 as a function of air temperature (T_{air}) and relative humidity (ϕ). All other influential parameters are kept constant which are: reflectivity and emissivity of water surface, Stanton number, and atmospheric pressure. The latter parameters are present in the correlations used in calculating the heat transfer components at the air–water interface, Section 2.6. As seen from Fig. 2, T_{eq} increases practically linearly with increasing T_{air} and ϕ.

Table 1 summarizes values of parameters used in Cases 1 through 4. These particular values comply with those used in the experimental measurements of Cerco [21]
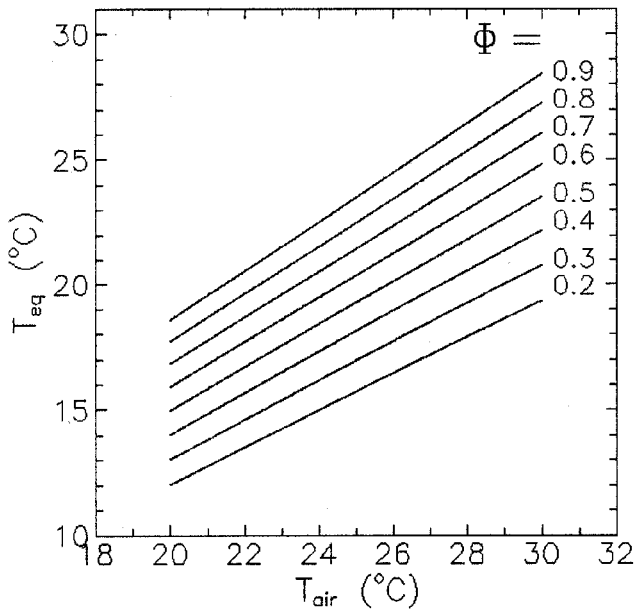
Fig. 2. Cooling pond equilibrium temperature variations with air temperature and relative humidity.

Table 1
Description and data relevant to experimental Cases 1 through 4, Cerco [21]

Case	$\dot{m}$ (kg/s)	Baffles	T_{eq} (°C)	T_i (°C)
1	0.284	Without	21.3[a]	46.3
2	0.284	With	21.3	47.1
3	0.568	Without	24.4	53.3
4	0.568	With	22.6	48.7

[a]Value was not reported and, hence, taken equal to that of Case 2.

for the purpose of comparison. Unless otherwise specifically mentioned, all other calculations are performed with T_i = 50°C and T_{eq} = 21.5°C, which correspond to T_{air} = 25°C and ϕ = 0.7.

It is recalled that the experiments of Cerco [21] were conducted under laboratory conditions. Details of wind speed and indoor conditions were not supplied in the study by Cerco [21]. Therefore, in the numerical model, calm wind conditions are considered which correspond to typical indoor laboratory conditions. Accordingly, relative velocity components between the moving water in the pond and the calm air are used in the shear stress and water evaporation rate at the air–water interface. The wind stresses, flow velocity, evaporation rate, etc. are determined iteratively by the numerical model. In real situations, the wind speed would likely enhance the relative velocity and hence increase the surface shear stresses and evaporation rate.

The rate of heat dissipated from the pond (q) is calculated from the equation as follows:

$$q = \dot{m}c_p\left(T_i - T_o\right) = \dot{m}c_p\Delta T_1 \tag{41}$$

where T_o is pond outlet temperature predicted by the model. From the calculated value of q, the pond mean effective heat-transfer coefficient (h_m) is determined from the equation as follows:

$$q = h_m A_s \left(T_m - T_{eq}\right) = h_m A_s \Delta T_2 \tag{42}$$

where T_m is the mean water temperature calculated by the model as a weighted average value. From Eq. (42), h_m is calculated and is, hence, based on the equilibrium temperature T_{eq}. The temperature differences ΔT_1 and ΔT_2 appearing in Eqs. (41) and (42) will be referred to in connection with varying $\dot{m}$ in Section 4.6.2.

It is interesting to note that h_m can also be determined from the local values of the heat transfer coefficient. The latter are the values calculated for all nodal points covering the pond. Denoting a typical node by indices i and j, h_m is determined as:

$$q_{i,j} = q_{i,j,e} + q_{i,j,r} + q_{i,j,c} = h_{i,j}A_{i,j}\left(T_{i,j} - T_{eq}\right) \tag{43}$$

where subscripts e, r, and c stand for evaporation, radiation, and convection, respectively. From Eq. (43), $h_{i,j}$ is evaluated, based on T_{eq}, and is used to determine h_m as follows:

$$h_m = \frac{1}{A_s}\int_{A_s} h \, dA_s = \frac{\sum\left(h_{i,j}A_{i,j}\right)}{\sum A_{i,j}} = \frac{\sum\left(h_{i,j}A_{i,j}\right)}{A_s} \tag{44}$$

Values of h_m evaluated from Eqs. (42) and (44) will be presented and compared as influenced by $\dot{m}$ in Section 4.6.2.

4.3. Grid independence study

Fig. 3 presents results of a grid independence study in which five grids are employed; namely, 9 × 10, 14 × 13, 20 × 17, 30 × 23, and 40 × 30 nodes in the x- and y-directions, respectively. Results presented are for dimensionless temperature (θ) and velocity (U) profiles at X = 0.5 for Case 2. It is noted that station X = 0.5 passes through the middle of the pond (x = 5.45 m) and across its width, see Fig. 1. Case 2 has the lower flow rate with baffles.

It is noted that the two coarsest grids produce results that show some grid effects, particularly for the velocity profiles, while the finest two grids give very close results and further grid refinement is therefore not warranted. The reason why grid effect with coarser grids is more pronounced on velocity variations than on temperature is due to the fact that the velocity varies significantly inside the pond as affected by the geometric configuration. This includes flow circulation and large velocity gradients which require finer grids. On the other hand, temperature is much more uniformly distributed than velocity. Velocity and temperature contours, constructed from the numerical results, are dealt with in Section 4.5.

With regard to grid effects on the pond overall quantities (e.g., overall pressure drop, total heat transfer rate, mean heat-transfer coefficient, water evaporation rate), all grids give very close results. It is decided that the 40 × 30 grid gives substantially grid-independent results and, therefore,
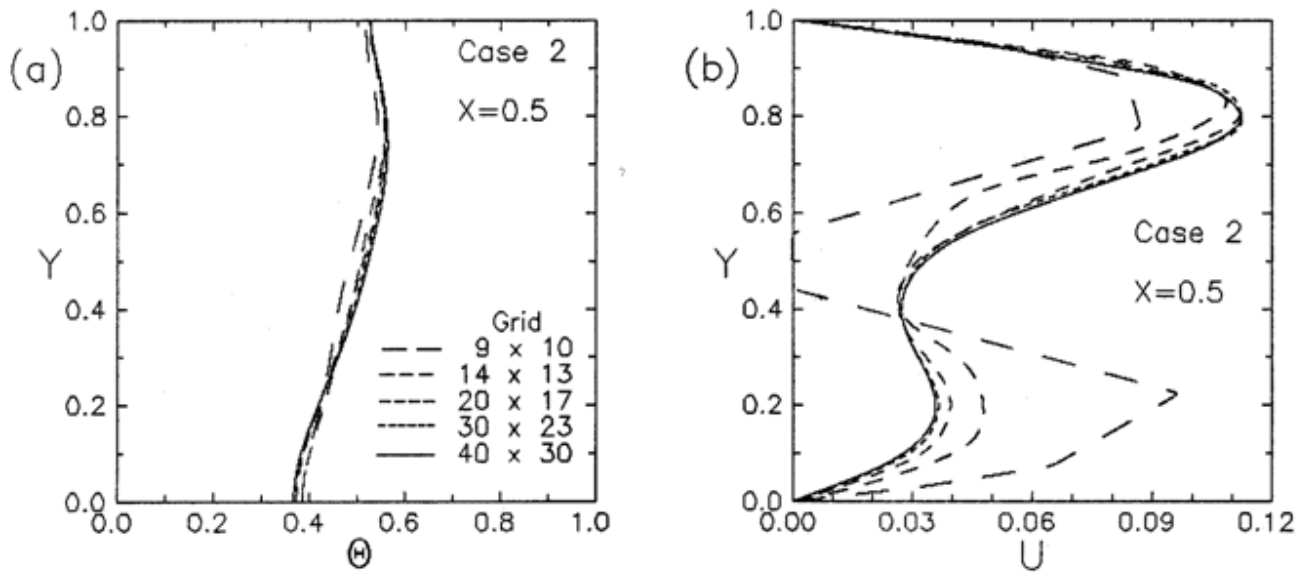
Fig. 3. Temperature and velocity profiles at middle of pond (X = 0.5) for Case 2 showing effect of using different finite-volume grid sizes.

is used throughout the study. Results obtained from such a grid converge in about 500 iterations and take a mere 3 s of computer time to execute on a personal computer (2.00 GHz).

4.4. Numerical model validation

Figs. 4a–d present dimensionless temperature profiles at the middle of the pond (X = 0.5) and across its width showing comparisons between present predictions and Cerco's [21] data for Cases 1 through 4, respectively. Comparisons are also made at other stations in the pond but are not presented here due to space limitation. Table 2 summarizes comparison between measured temperatures and present predicted values for Case 2. It is noted that the percentage difference is given with reference to ($T_i - T_{eq}$), where T_i = 47.1°C and T_{eq} = 21.3°C. It is concluded that the agreement between predictions and measurements is, in general, quite good. Further comparisons between model predictions and Cerco's data as well as with the 1-D closed form analytical solutions are shown in Section 4.6.4 when results considering pond cooling capacity are presented.

4.5. Flow pattern and detailed temperature distribution

Detailed numerical results in terms of streamline plots, speed contours, and temperature contours are displayed and discussed in the appendix for Cases 1–4.

4.6. Effect of mass flow rate on hydrodynamic and thermal characteristics

4.6.1. Effect of $\dot{m}$ on pressure drop and loss coefficient

Fig. 5a presents the variation of the pressure drop between pond inlet and outlet (Δp) with the mass flow rate ($\dot{m}$). As seen, Δp increases with $\dot{m}$ and that, for a given $\dot{m}$,

the presence of baffles increases Δp but only little. The corresponding pressure loss coefficient (C_{PL}) is seen to be practically constant with varying $\dot{m}$, Fig. 5b.

4.6.2. Effect of $\dot{m}$ on heat transfer rate, mean temperature, and heat transfer coefficient

Figs. 6a–d present effects of $\dot{m}$ on, respectively, pond heat transfer rate (q), pond mean and outlet temperatures (T_m and T_o), mean heat-transfer coefficient (h_m), and temperature differences (ΔT). As seen from Fig. 6a, q increases with $\dot{m}$. This feature might not have been so obvious but for the fact that all temperatures in the pond do increase with increasing $\dot{m}$ in which case all components of heat transfer at the air–water interface are enhanced due to increase in corresponding temperature differences. A convenient representative temperature in the pond is the mean pond temperature (T_m). This is calculated as a weighted average and plotted vs. $\dot{m}$ in Fig. 6b. The pond outlet temperature (T_o), which is the inlet temperature to the condenser, is also shown for reference. It is seen that T_m as well as T_o increase with $\dot{m}$; the increase is fast at the beginning and gets more gradual at higher $\dot{m}$. These values would reach asymptotically the inlet temperature (T_i = 50°C) at much larger $\dot{m}$, in which the pond would approach its ultimate operating capacity and yield its maximum possible heat transfer rate.

Based on q, A_s, T_m, and T_{eq}, the pond mean heat-transfer coefficient (h_m) is determined from Eq. (42) and plotted vs. $\dot{m}$ in Fig. 6c. As seen, h_m increases with $\dot{m}$ and that, for a given $\dot{m}$, the presence of baffles enhances the performance of the pond by giving higher effective heat-transfer coefficient. Values of h_m as calculated from Eq. (44) are found to be very close to those presented in Fig. 6c, and hence are not presented for clarity reason. It is, therefore, concluded that the two different methods of determining h_m, cf. Eqs. (42) and (44), produce effectively the same results.
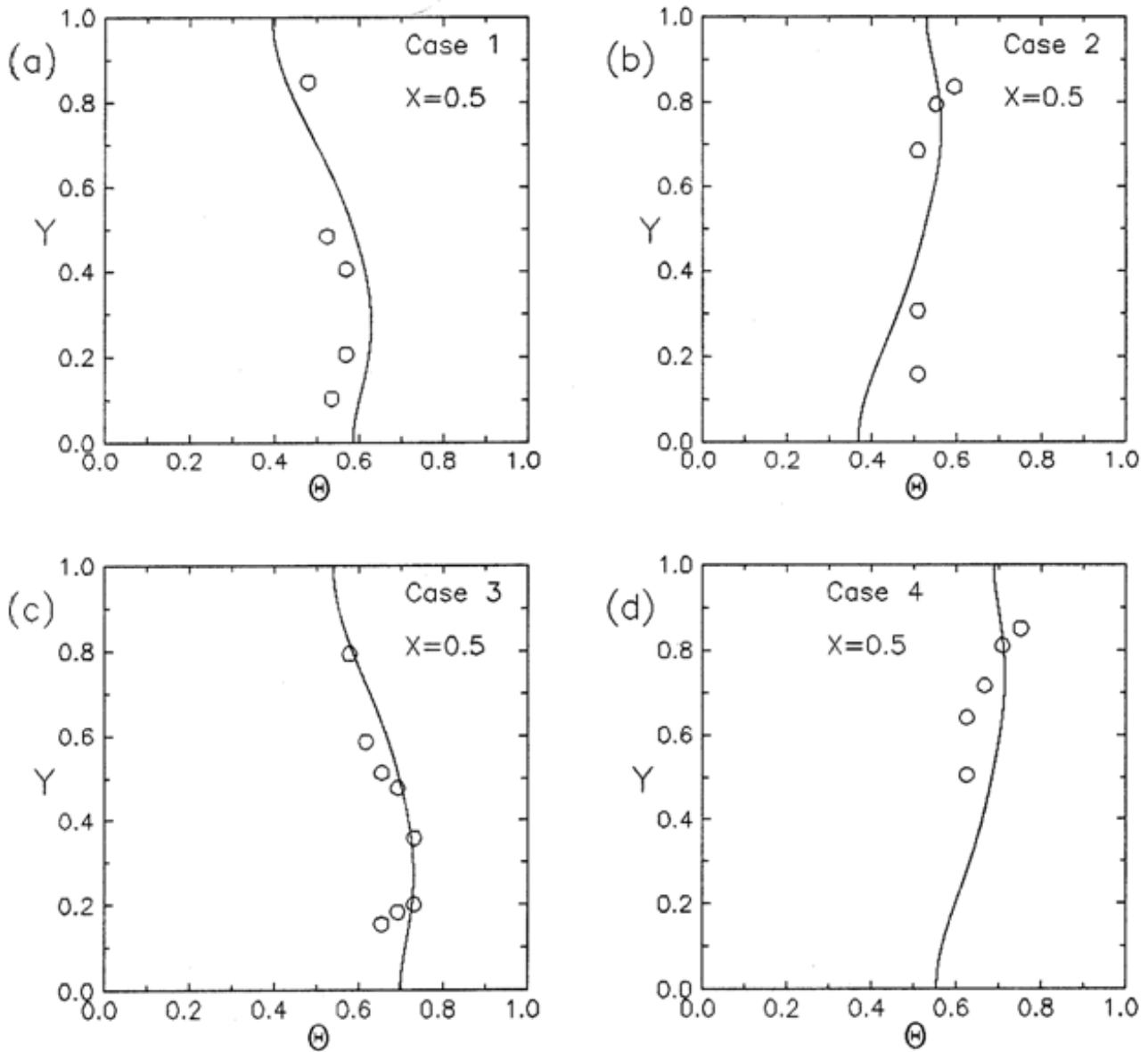
Fig. 4. Temperature profiles at middle of pond ($X = 0.5$) for Cases 1 through 4 showing comparison between predictions (lines) and measurements (Cerco [21]) (circles).

Table 2
Comparison between measured temperatures (Cerco [21]) and present numerical simulation for Case 2; $X = 0.5$, $T_i = 47.1°C$, and $T_{eq} = 21.3°C$

Y	θ Exp.	θ Num.	T (°C) Exp.	T (°C) Num.	% Diff.[a]
0.16	0.51	0.41	34.5	31.9	10.1
0.31	0.51	0.46	34.5	33.2	5.0
0.69	0.51	0.56	34.5	35.7	–4.7
0.79	0.56	0.57	35.7	36.0	–1.2
0.83	0.60	0.56	36.8	35.7	4.3

[a] % Diff. $= \dfrac{T_{exp} - T_{num}}{T_i - T_{eq}} \times 100$.

Fig. 6d shows that while ΔT_2 ($= T_m - T_{eq}$) increases with $\dot{m}$, the opposite is true for ΔT_1 ($= T_i - T_o$). The latter is caused by increasing T_o with $\dot{m}$ (Fig. 6b) while T_i is constant. However, despite ΔT_1 decreases with increasing $\dot{m}$, the product $\dot{m} \Delta T_1$ increases with $\dot{m}$. Of course, $\dot{m} \Delta T_1$ times c_p is the same q as presented in Fig. 6a. An important conclusion is drawn here and that is operating the pond at as high a flow rate as practically possible is an advantage. This is explained by the fact that all components of heat transfer at the pond air–water interface get enhanced by increasing $\dot{m}$, and hence the ultimate heat rejected by the pond is enhanced. Nevertheless, the pressure drop of cooling water passing through the condenser tubes would increase with increasing $\dot{m}$. Therefore, a compromise must be made between these two conflicting requirements and the designer may optimize
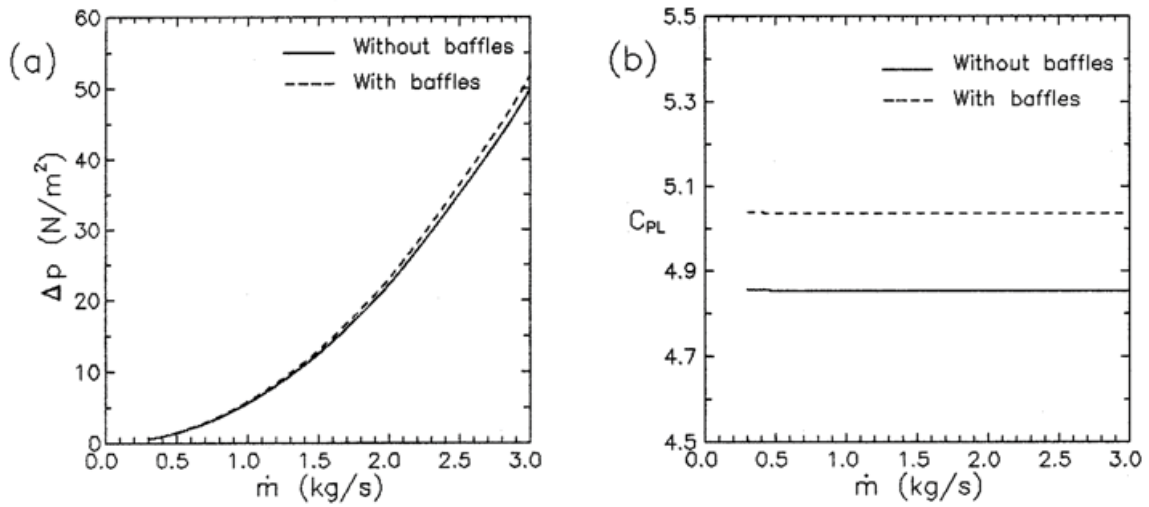
Fig. 5. Effect of mass flow rate on (a) pressure drop between pond inlet and outlet, and (b) pressure loss coefficient.
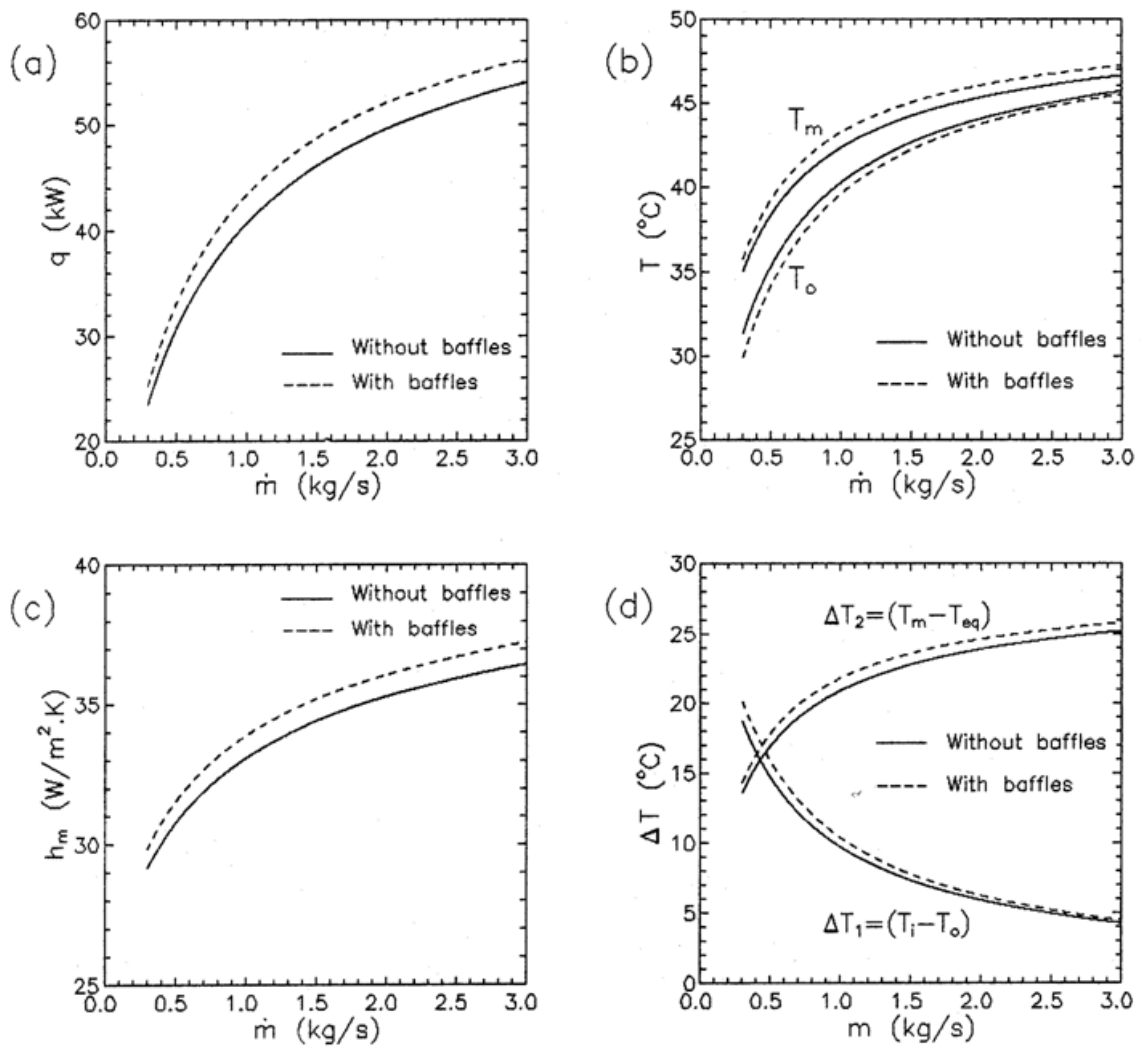

Fig. 6. Effect of mass flow rate on (a) total heat transfer rate, (b) mean and outlet temperatures, (c) mean heat-transfer coefficient, and (d) ΔT_1 and ΔT_2.

among alternatives of higher flow rates with corresponding smaller ΔT_1 and vice versa.

With reference to Fig. 6a, Table 3 summarizes effect of $\dot{m}$ on total heat transfer rate from pond (q) for the cases of without and with baffles. Percentage increase in q through use of baffles is shown for every $\dot{m}$.

4.6.3. Effect of $\dot{m}$ on evaporation rate

Of interest too is the amount of water evaporated from the pond surface. This is calculated and presented in terms of column of water evaporated in mm per day (z_e) vs. $\dot{m}$ in Fig. 7a. As seen, z_e increases with $\dot{m}$ and more water is evaporated for the case of pond with baffles. Of course, more evaporation means more heat transfer and hence more heat rejected from the pond. While this is the objective of evaporative cooling, makeup water must, therefore, be supplied. This will cause a problem in regions where water is not available in sufficient quantity. The situation might get more difficult in dry climates where more evaporation would take place as

the relative humidity gets lower. Further account on this is given in Section 4.7 when the relative humidity is varied.

In addition, it is interesting to compare the percentage values of the heat-transfer components among each other and as affected by $\dot{m}$. The results are displayed in Fig. 7b from which two features are extracted; first, the heat transfer by evaporation is the dominant component with about 70% (note the logarithmic scale); this is followed by net radiation loss with nearly 20%, and just above 10% for natural convection; the forced convection component is much less 1%. The second feature is that these percentage components do not vary much with $\dot{m}$, except for the forced convection albeit can be neglected. It should be emphasized, however, that each of these component increases with $\dot{m}$ but the percentage change is much less sensitive to $\dot{m}$.

4.6.4. Pond cooling capacity

For a given geometric configuration, the pond thermal performance is assessed by a unique relationship between pond dimensionless outlet temperature θ_o [$\theta_o = (T_o - T_{eq})/(T_i - T_{eq})$] and pond cooling capacity r ($r = h_m A_s/\dot{m}c_p$) as displayed in Fig. 8. The experimental results of Cerco [21] are shown for comparison. The 1-D closed-form analytical solutions for the cases of fully mixed and no mixing (plug flow) ponds are also shown which represent two extreme theoretical limits on cooling pond performance that should encompass all results with finite mixing. The latter results are not shown on the figure for clarity reason. The plug flow pond provides the best performance and the fully mixed pond provides the worst performance. It is noted that θ_o decreases with increasing r which signifies that lower pond outlet temperature can be achieved at higher pond cooling capacity. The latter can also be affected by increasing pond surface area, a parameter which is fixed in the present study. It is interesting to note that the pond with baffles gives better performance compared with that without baffles. This can also be noted from the experimental data though these are little scattered as might well be

Table 3
Effect of mass flow rate ($\dot{m}$) on total heat transfer rate from pond (q) showing enhancement of q through use of baffles; $T_i = 50°C$ and $T_{eq} = 21.5°C$

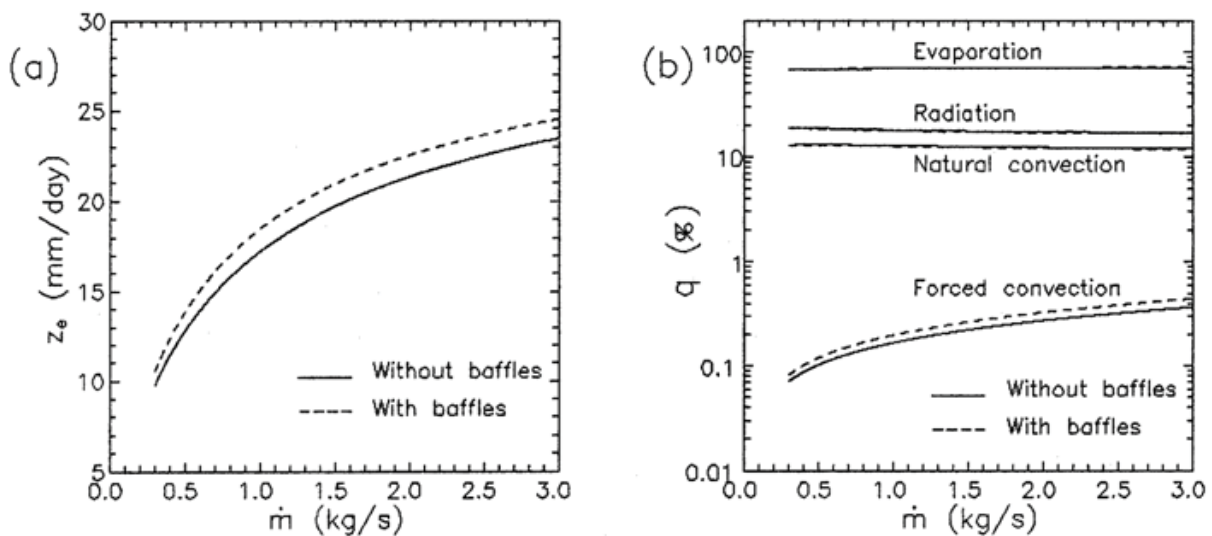| $\dot{m}$ (kg/s)	q (kW) without baffles	q (kW) with baffles	% Increase
0.3	23.38	25.17	7.66
0.4	27.42	29.55	7.77
0.5	30.64	33.01	7.73
0.7	35.56	38.18	7.37
1.0	40.67	43.38	6.66
1.5	46.10	48.73	5.71
2.0	49.61	52.09	5.00
3.0	53.99	56.20	4.10

Fig. 7. Effect of mass flow rate on (a) evaporation rate, and (b) percentage heat transfer rates by various components.
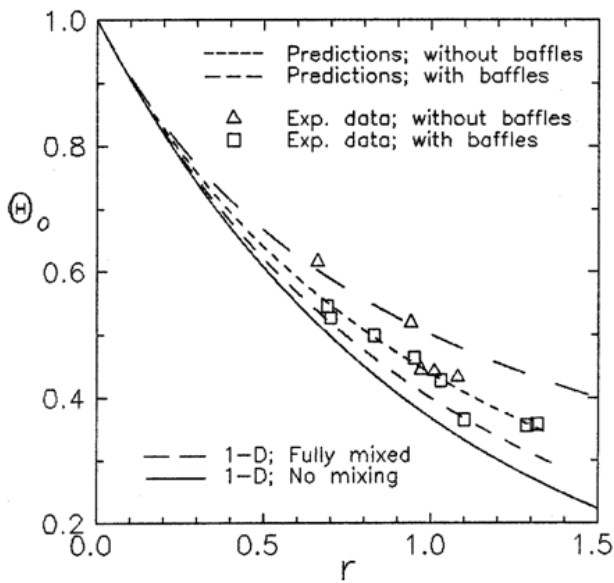
Fig. 8. Variation of pond outlet temperature with pond cooling capacity showing comparisons between predictions, measurements (Cerco [21]), and 1-D idealized exact solutions.

Fig. 10. Effect of relative humidity on temperature profile at middle of pond ($X = 0.5$) for $\dot{m} = 1$ kg/s; with baffles.

expected. As far as the comparison between predictions and measurements is concerned, this may be judged to be generally very good, except for two data points which look little extreme by lying on top or even little above the 1-D fully mixed results.

4.7. Effect of relative humidity on thermal characteristics

All results presented above are for a relative humidity $\phi = 0.7$. Fig. 9a shows the effect of ϕ on z_e as influenced by varying pond mean temperature (T_m). It is clear that, for a given ϕ, the evaporation rate (in terms of z_e) increases with
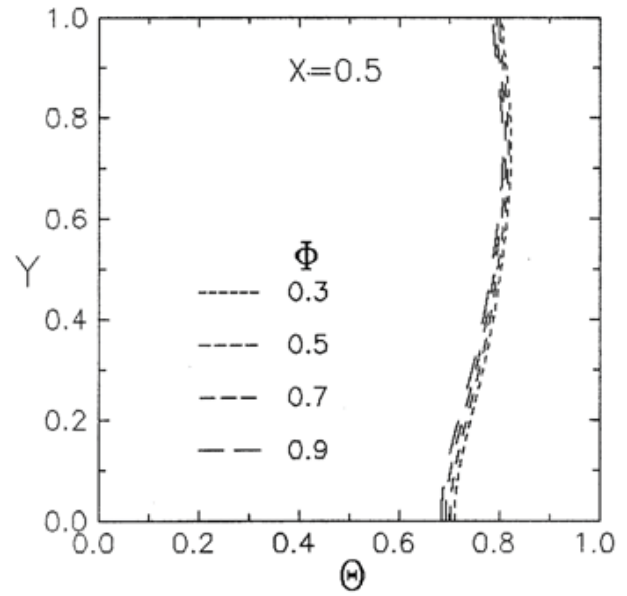
T_m as to be expected. This is since higher pond temperature gives higher saturation water-vapor-pressure and hence increases the driving force of the evaporation process. For a given T_m, on the other hand, z_e increases with decreasing ϕ. This is because decreasing ϕ decreases the partial water vapor pressure in the ambient air and hence, likewise, increases the driving force of the evaporation process. All these results are calculated for $T_i = 50°C$ and $T_{air} = 25°C$. It is quite obvious that more makeup water would be required in dryer climates for a given water temperature. However, the advantage of that is a higher heat rejection from the pond as can be appreciated from the corresponding results for q as presented in Fig. 9b. In other words, the condenser
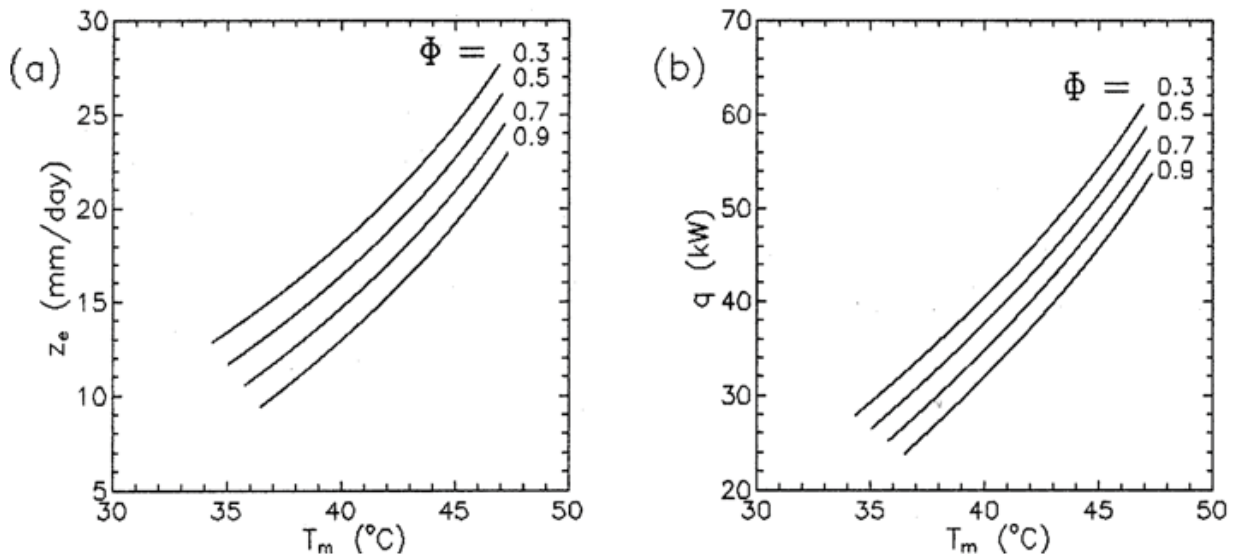

Fig. 9. Effect of pond mean temperature and relative humidity on (a) evaporation rate and (b) total heat transfer rate; with baffles.

of a power plant would better operate in dryer climates when cooling is effected by cooling ponds and, likewise, by cooling towers.

Fig. 10 examines the sensitivity of water temperature to relative humidity in which dimensionless temperature profiles at the middle of pond ($X = 0.5$) are plotted at different values of ϕ. These results are calculated for the pond with baffles at $\dot{m} = 1$ kg/s, $T_i = 50$°C, and $T_{air} = 25$°C, as a representative case. In terms of θ defined based on T_{eq}, it is quite interesting to note that θ variation dependence on ϕ is very weak. This finding gives further support to the results presented earlier in Fig. 4, in which comparisons between predictions and measurements were made, rendering such results to be less sensitive to relative humidity.

5. Summary and conclusions

A depth-integrated CFD model, based on the finite-volume method, was developed and applied to calculate detailed velocity and temperature distributions inside shallow experimental cooling pond. The numerical model was validated by comparing results with available temperature measurements. Effects of mass flow rate ($\dot{m}$) on pond hydrodynamic and thermal characteristics for cases of without and with internal baffles were investigated. Results showed that pressure loss coefficient remained constant, while pressure drop between pond inlet and outlet increased with increasing $\dot{m}$. Heat dissipated from the pond increased with $\dot{m}$ despite the decrease in difference between water inlet and outlet temperatures.

Pond effective heat-transfer coefficient, mean temperature, and water loss by evaporation were determined as a function of $\dot{m}$ and relative humidity (ϕ). Outlet temperature was determined as a function of pond cooling capacity. Streamline plots showed that flow pattern was independent of $\dot{m}$ but was strongly dependent on geometric configuration. A single contour map of normalized speed was, therefore, sufficient to describe all speeds inside the pond for different $\dot{m}$. It is recommended that $\dot{m}$ should be as high as possible in order to enhance heat loss from pond surface but this would increase pumping power of cooling water through condenser tubes in which a compromise must be sought.

Future work will consider applying the validated mathematical model to larger size ponds under real environmental conditions.

Acknowledgment

Symbols

A_s	—	Pond surface area, m^2
C_{PL}	—	Pressure loss coefficient
c_p	—	Specific heat, J/kg K
h_m	—	Mean effective heat-transfer coefficient, W/m^2 K
k	—	Thermal conductivity, W/m K
L	—	Length of pond (m), or latent heat of vaporization, J/kg
M	—	Mass flux at air–water interface, kg/m^2 s
m	—	Mass fraction of water vapor in air
$\dot{m}$	—	Mass flow rate, kg/s
N, S, E, W, P	—	Nodal points
p	—	Pressure, N/m^2 or mbar
q	—	Pond total heat-transfer rate, W or kW
q''	—	Heat flux component, W/m^2
r	—	Dimensionless pond cooling capacity
S	—	Source/sink term
St	—	Stanton number, St $= h/\rho_{air} \cdot V_{rel} \cdot c_p$
T	—	Temperature, °C or K
U	—	Dimensionless velocity, $U = u/u_i$
U_o, V_o	—	Wind velocity relative to water velocity, in x- and y-directions, m/s
u, v	—	Velocity components in x- and y-directions, m/s
V_{rel}	—	Relative velocity of wind and water, $V_{rel} = (U_o^2 + V_o^2)^{1/2}$, m/s
W	—	Width of pond, m
X	—	Dimensionless distance, $X = x/L$
x, y	—	Coordinate directions along length and width of pond, m
Y	—	Dimensionless distance, $Y = y/W$ or $Y = y/L$
z	—	Depth of water, m
z_e	—	Water evaporated, mm/d

Greek

α	—	Dispersion coefficient (thermal diffusivity), m^2/s
Γ	—	Exchange (diffusion) coefficient, N s/m^2
ε	—	Surface emissivity
θ	—	Dimensionless temperature, $\theta = (T - T_{eq})/(T_i - T_{eq})$
μ	—	Viscosity, N s/m^2
ρ	—	Density, kg/m^3
σ_T	—	Turbulent Prandtl number, $\sigma_T = c_p \mu_{eff}/k_{eff}$
ϕ	—	General dependent variable or relative humidity

Subscripts

c	—	Convection
e	—	Evaporation
eff	—	Effective
eq	—	Equilibrium
i	—	Inlet
m	—	Mean
o	—	Outlet
s	—	Surface
sur	—	Surroundings

Superscripts

-	—	Depth averaged (integrated) quantity

References

[1] S.A. Lowe, Improving the performance of power plant cooling ponds, J. Environ. Manage., 105 (2012) 90–95.

[2] N. Voutchkov, Overview of seawater concentrate disposal alternatives, Desalination, 273 (2011) 205–219.

[3] T.M. Missimer, B. Jones, R.G. Maliva, Intakes and Outfalls for Seawater Reverse-Osmosis Desalination Facilities: Innovations and Environmental Impacts, Springer International Publishing, Switzerland, 2015.

[4] P. Balasubramanian, A brief review on best available technologies for reject water (brine) management in industries, Int. J. Environ. Sci., 3 (2013) 2010–2018.

[5] K. Elsaid, N. Bensalah, A. Abdel-Wahab, Inland Desalination: Potentials and Challenges, Z. Nawaz, Ed., Advances in Chemical Engineering, ISBN: 978-953-51-0392-9, InTech, London, UK, 2012, pp. 449–480. Available at: https://www.intechopen.com/books/advances-in-chemical-engineering/inland-desalination-potentials-and-challenges.

[6] E. González, B. Arconada, P. Delgado, A. Alcaraz, A. Álvarez, M. Antequera, Y. Fernández, A. Garrote, S. de Rico, E. Salete, J.L.S. Lizaso, Environmental research on brine discharge optimization: a case study approach, Desal. Wat. Treat., 31 (2011) 197–205.

[7] A.G. Christianson, F.H. Rainwater, M.A. Shirazi, B.A. Tichenor, Reviewing Environmental Impact Statements - Power Plant Cooling Systems, Engineering Aspects, National Thermal Pollution Research Program, Pacific Northwest Environmental Research Laboratory, EPA, NERC-Corvallis, Oregon, 1973.

[8] K. Dyer, P. Holmes, S. Roast, C.J.L. Taylor, A. Wither, Challenges in the management and regulation of large cooling water discharges, Estuarine Coastal Shelf Sci., 190 (2017) 23–30.

[9] M. Watanabe, J.J. Connor, Mathematical modelling of a stratified cooling pond, Appl. Math. Modell., 1 (1976) 97–100.

[10] M. Ahmed, W.H. Shayya, D. Hoey, A. Mahendran, R. Morris, J. Al-Handaly, Use of evaporation ponds for brine disposal in desalination plants, Desalination, 130 (2000) 155–168.

[11] T. Bleninger, G.H. Jirka, Modelling and environmentally sound management of brine discharges from desalination plants, Desalination, 221 (2008) 585–597.

[12] W. Wei, Z. Zhang, Y. Zheng, Y. Liu, Numerical simulation of additional guiding baffles to improve velocity distribution in an oxidation ditch, Desal. Wat. Treat., 57 (2016) 24257–24266.

[13] Y. Liu, P. Zhang, W. Wei, Simulation of effect of a baffle on the flow patterns and hydraulic efficiency in a sedimentation tank, Desal. Wat. Treat., 57 (2016) 25950–25959.

[14] H.A. Hussein, R. Abdullah, S. Harun, M. Abdulkhaleq, Numerical model of baffle location effect on flow pattern in oil and water gravity separator tanks, World Appl. Sci. J., 26 (2013) 1351–1356.

[15] N.M. Ogarekpe, J.C. Agunwamba, Effect of geometry on the performance of integrated solar and hydraulic jump enhanced waste stabilization pond, Desal. Wat. Treat., 57 (2016) 24946–24959.

[16] S.A. Kalogirou, Seawater desalination using renewable energy sources, Prog. Energy Combust. Sci., 31 (2005) 242–281.

[17] M. Giestas, H. Pina, A. Joyce, The influence of radiation absorption on solar pond stability, Int. J. Heat Mass Transfer, 39 (1996) 3873–3885.

[18] M. Giestas, A. Joyce, H. Pina, The influence of non-constant diffusivities on solar ponds stability, Int. J. Heat Mass Transfer, 40 (1997) 4379–4391.

[19] F. Suárez, S.W. Tyler, A.E. Childress, A fully coupled, transient double-diffusive convective model for salt-gradient solar ponds, Int. J. Heat Mass Transfer, 53 (2010) 1718–1730.

[20] E. Sartori, A critical review on equations employed for the calculation of the evaporation rate from free water surfaces, Sol. Energy, 68 (2000) 77–89.

[21] C.F. Cerco, Experimental and Analytical Study of the Design of Shallow Cooling Ponds, M.Sc Thesis, Department of Civil Engineering, Massachusetts Institute of Technology, Boston, USA, 1977.

[22] C.B. Vreugdenhil, Numerical Methods for Shallow-Water Flow, Kluwer Academic Publishers, Dordrecht, The Netherlands, 1994.

[23] S.V. Patankar, Numerical Heat Transfer and Fluid Flow, Hemisphere Publishing Corporation, Washington, 1980.

[24] S.V. Patankar, D.B. Spalding, A calculation procedure for heat, mass and momentum transfer in three-dimensional parabolic flows, Int. J. Heat Mass Transfer, 15 (1972) 1787–1806.

[25] D.B. Spalding, Transfer of Heat in Rivers, Bays, Lakes and Estuaries—THIRBLE, Report No. HTS/75/4, Department of Mechanical Engineering, Imperial College of Science and Technology, London, UK, 1975.

[26] H. Glaser, E. Pruckner, Heat Transfer Between the Surface of a River and the Atmosphere, International Heat Transfer Conference, 6th, Toronto, Canada, 1978, pp. 49–54.

[27] H. Glaser, E. Pruckner, Heat and Mass Transfer to Rivers, International Heat Transfer Conference, 7th, Munich, Germany, 1982, pp. 301–322.

[28] J.S. Maulbetsch, J.A. Bartz, Cooling Towers and Cooling Ponds, Chapter 10, Handbook of Heat Transfer Applications, 2nd ed., W.M. Rohsenow, J.P. Hartnett, E.N. Ganic, Eds., McGraw Hill, New York, 1985.

Appendix: streamlines, speed, and temperature contours

Detailed numerical results are presented in Figs. A1–A3. Figs. A1a and A1b depict the flow patterns inside the pond via streamlines presented along with normalized stream-function values (with respect to $\dot{m}$) for the cases without and with baffles, respectively. The results shown are Reynolds number independent and hence represent all flow rates used. It is clear from Fig. A1a that the flow "short-circuits" the pond, where the total mass flow rate entering and leaving is confined in the region bound by the two streamlines identified with stream function values of 0 and 1. The flow path of a massless particle released at the pond inlet and exiting at the outlet port is very short compared with the pond perimeter. The entering and exiting mass generates a large recirculation zone which occupies nearly one quarter of the pond total surface area. This zone
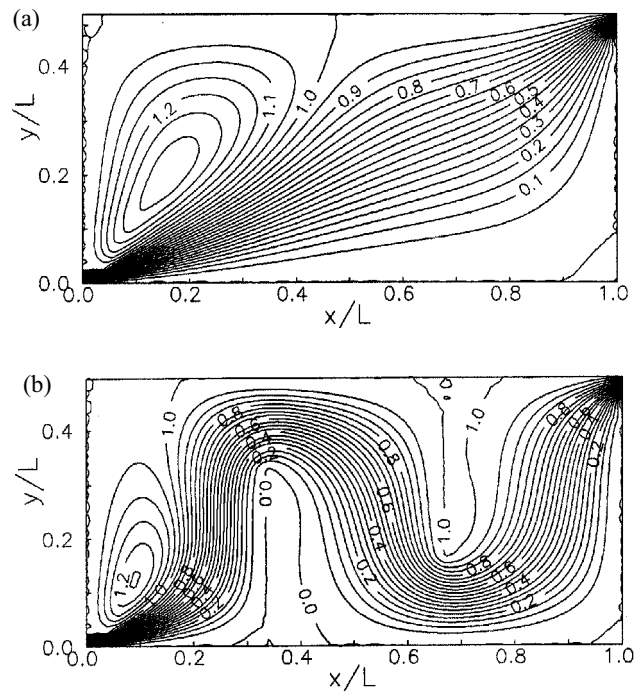

Fig. A1. Streamlines and stream-function values normalized by $\dot{m}$; (a) without baffles and (b) with baffles.

is seen enclosed by the streamline identified with the stream function value of 1 and the pond side walls. A much smaller recirculation region is shown enclosed by the streamline identified with the stream function value of 0 and the pond side walls at the opposite corner (bottom right corner in the figure). By introducing internal baffles, the flow pattern completely changes as depicted in Fig. A1b. The flow path is very much elongated as compared with the case with no baffles. Accordingly, the thermal performance is improved by better utilization of the surface area available in the pond. Such improvements are assessed in the results presented in Section 4.6.

Figs. A2a and A2b present the corresponding speed contours with values normalized by u_i for the cases without and with baffles, respectively. Again, these results are Reynolds number independent. Such maps of speed contours can be used to generate actual speed distribution inside the pond for any $\dot{m}$ simply by multiplying the contour values shown by corresponding u_i.

Figs. A3a–A3d present the dimensionless temperature contours for Cases 1–4, respectively. These contours give an overall picture of the temperature distributions in the pond under different conditions. It may be noted that the contours are similar (but with different values) for Cases 1 and 3 and for Cases 2 and 4.
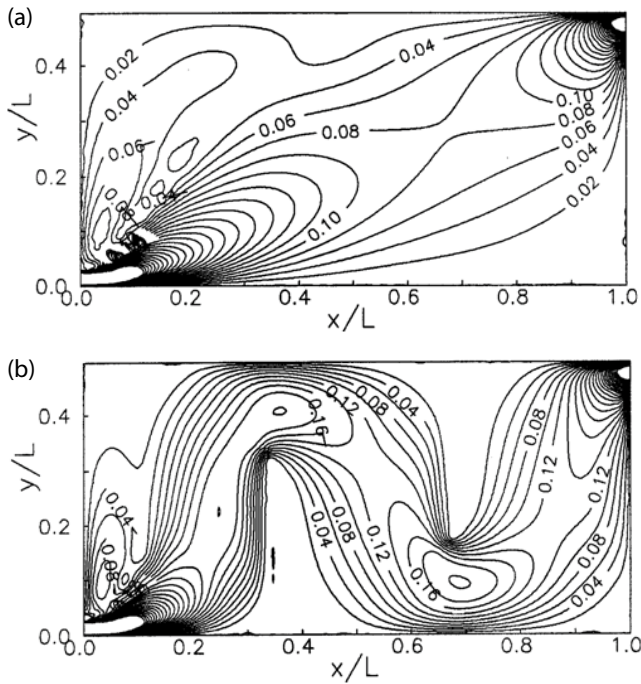

Fig. A2. Speed contours with values normalized by u_i; (a) without baffles and (b) with baffles.
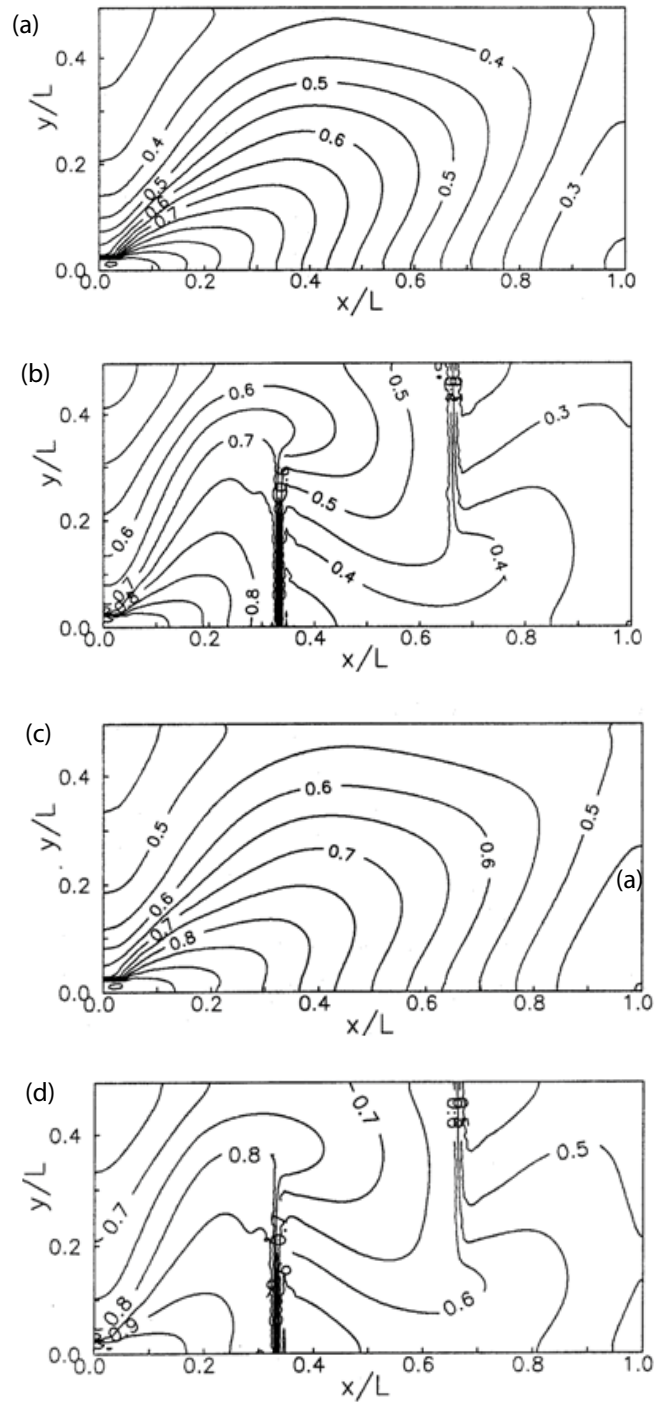

Fig. A3. Dimensionless temperature contours for Cases 1 through 4; (a) through (d), respectively.